



Audible enclaves crafted by nonlinear self-bending ultrasonic beams

Jia-Xin Zhong^{a,1}, Jun Ji^{a,1}, Xiaoxing Xia^b, Hyeonu Heo^a, and Yun Jing^{a,2}

Edited by Michael Berry, University of Bristol, Bristol, United Kingdom; received May 5, 2024; accepted January 31, 2025

Delivering audible content to a targeted listener without disturbing others is paramount in audio engineering. However, achieving this goal has long been challenging due to the diffraction of low-frequency (long-wavelength) audio waves in linear acoustics. Here, we introduce an approach for creating remote audio spots, dubbed audible enclaves, by harnessing the local nonlinear interaction of two self-bending ultrasonic beams with distinct spectra. The self-bending ultrasonic beams created by acoustic metasurfaces, though inaudible, can bypass obstacles such as human heads. At their intersection behind obstacles, highly localized audible enclaves are formed due to the local nonlinear interactions. Additionally, we demonstrate the ultrabroadband capabilities of our metasurface-based implementation both numerically and experimentally, spanning from 125 Hz to 4 kHz (6 octave bands), covering the majority of the audible frequency range. The practicality of our proposed technique is underscored by its compact implementation size (0.16 m, equivalent to 0.06 wavelengths at 125 Hz), as well as its robust performance under wideband transient audio signal excitation and in a common room with reverberations. Our proposed audible enclaves hold significant potential for various applications in advanced audio engineering, including private speech communications, immersive spatial audio reproduction, and high-resolution sound/quiet zone control.

self-bending beams | nonlinear acoustics | metasurface | sound/quiet zone control | spatial audio

Recent advancements in digital signal processing and loudspeaker array design have significantly enhanced audio engineering capabilities to manipulate and reproduce sound with precision and fidelity, thus enabling immersive audio experiences that profoundly impact various aspects of human life (1–8). The ultimate goal of modern sound reproduction over multiple zones is to deliver personalized, interface-free audio to multiple listeners, minimizing disruptions to other areas, all without requiring physical isolation or the use of wearable devices like headphones (4). Real-world applications often involve creating personal sound or quiet zones within complex acoustic reverberant environments, such as rooms and car cabins, where challenges arise from reflections from walls and scattering by obstacles like human heads. Overcoming these challenges is essential for applications such as private speech communications and achieving spatial audio that is free from crosstalk and spillover effects, as well as for effective active noise control (9–14).

Self-bending beams, a recent focus of advanced waveform engineering, offer potential solutions to these issues. These peculiar beams, whether acoustic or electromagnetic, can follow curved trajectories, navigate around obstacles, and withstand perturbations (15–20). Their unique properties have led to applications such as contactless manipulation of objects (17, 21–23) and noninvasive biomedical imaging (19). Notably, in audio engineering, self-bending beams have been demonstrated to deliver audio content around human heads (24). However, due to the diffraction properties of long-wavelength audio waves, bulky sound sources and costly digital signal processing platforms are typically required. For instance, experiments in ref. 24 required a source size of 2.6 m to bypass a human head with a radius of 0.1 m at 4 kHz (wavelength is 8.6 cm), accompanied by extensive signal processing across 64 channels. Implementing such techniques for audio frequencies as low as 100 Hz (wavelength is 3.43 m) entails greater challenges, including not only the need for even larger source sizes but also increased susceptibility to acoustic reverberations in common rooms, attributed to longer wavelengths (11, 25). Moreover, the sound along the beam's trajectory remains audible, which is undesirable in many applications where privacy is crucial. In essence, the diffraction of acoustic waves imposes a fundamental physical constraint on the further development of the cutting-edge audio engineering techniques.

Various linear-acoustics-based methods, including metamaterials (26–28), superoscillation (29), and time reversal focusing (30), have been proposed to overcome the

Significance

Recent advancements in digital signal processing and loudspeaker array design have enabled us to experience immersive spatial audio in virtual/augmented/extended reality environments in our daily lives. However, further development in audio engineering is impeded by physical constraints stemming from the diffraction of long-wavelength audio waves. This study introduces an approach to address this issue by showcasing the creation of ultrabroadband (125 Hz to 4 kHz) and highly localized remote audio spots, referred to as audible enclaves. By marrying local acoustic nonlinearity with inaudible self-bending ultrasonic beams, the proposed technique overcomes the physical limits in linear acoustics, paving the way for possibilities in future audio engineering.

Author affiliations: ^aGraduate Program in Acoustics, College of Engineering, The Pennsylvania State University, University Park, PA 16802; and ^bLawrence Livermore National Laboratory, Livermore, CA 94550

Author contributions: J.-X.Z., J.J., and Y.J. designed research; J.-X.Z., J.J., and X.X. performed research; J.-X.Z. analyzed data; and J.-X.Z., J.J., H.H., and Y.J. wrote the paper.

The authors declare no competing interest.

This article is a PNAS Direct Submission.

Copyright © 2025 the Author(s). Published by PNAS. This article is distributed under Creative Commons Attribution-NonCommercial-NoDerivatives License 4.0 (CC BY-NC-ND).

¹J.-X.Z. and J.J. contributed equally to this work.

²To whom correspondence may be addressed. Email: yqj5201@psu.edu.

This article contains supporting information online at <https://www.pnas.org/lookup/suppl/doi:10.1073/pnas.2408975122/-DCSupplemental>.

Published March 17, 2025.

diffraction of acoustic waves. Recently, a new approach leveraging nonlinear acoustics has been introduced to further enhance the subdiffraction control of acoustic waves (31). Nonlinear effects are ubiquitous in acoustics due to the inherent nonlinear nature of the governing acoustic wave equation (32). For the most common quadratic nonlinearity in acoustics, when two primary waves with different frequencies f_1 and f_2 are emitted, a second-order nonlinear component, known as the difference-frequency wave (DFW), is generated at frequency $f = |f_1 - f_2|$. This strategic maneuver allows bypassing the diffraction limit typically imposed on the DFW in linear acoustics, and it becomes particularly interesting for audio engineering applications when the DFW falls within the audible frequency range, while primary waves are inaudible ultrasonic beams.

There are two distinct types of nonlinear acoustic effects: cumulative and local nonlinear effects. Cumulative nonlinearity stems from the nonlinear parameter of a specific medium, with various applications including biomedical imaging (33, 34) and parametric arrays (35–37). However, local nonlinearity, determined by the local Lagrangian density of primary waves, is often overlooked (32, 33, 38). Neither of these two nonlinear acoustic effects has been explored in conjunction with self-bending beams in acoustics, making it uncharted territory.

Here, we conceptualize, implement, and demonstrate the creation of audible enclaves enabled by local nonlinear interaction between two ultrasonic self-bending beams created by subwavelength metasurfaces and sources, overcoming the fundamental limit set by diffraction effects in linear acoustics. We showcase the beams' ability to circumvent obstacles, such as a cylinder or a human head, and form a highly localized audible enclave behind the obstacle, while maintaining inaudible trajectories. The generation of the self-bending beams is facilitated by 3D-printed acoustic metasurfaces. Although acoustic metasurfaces are typically associated with narrow frequency bands in the domain of linear acoustics (11, 39), this study shows that, remarkably, they can attain ultrabroadband performance, ranging from 125 Hz to 4 kHz (6 octave bands), when employed in the nonlinear acoustic regime. This is because manipulating waves within a narrow band at ultrasound frequencies (e.g., 10% bandwidth at 40 kHz) can translate to a broad frequency range in the audio domain ($40 \text{ kHz} \times 10\% = 4 \text{ kHz}$). Our compact implementation with a source aperture size of only 0.16 m, equivalent to 0.06 wavelengths at 125 Hz, highlights its superiority compared to the linear-acoustics-based approach (24). Furthermore, observation of audible enclaves under transient wideband audio signal excitation in a common room demonstrates the technique's robustness to acoustic reverberations. Our proposed technique integrates self-bending beams, nonlinear acoustics, and metasurfaces, offering possibilities for future advancements in audio engineering.

Results

Creation of Audible Enclaves by Nonlinear Self-Bending Beams. Fig. 1 depicts the schematic of our proposed concept for creating audible enclaves by harnessing nonlinear self-bending beams. We employ two acoustic sources emitting ultrasonic waves at frequencies f_1 and f_2 , each covered by metasurfaces to facilitate the generation of self-bending ultrasonic beams and the formation of an intersection zone behind an obstacle (illustrated as a human head in Fig. 1). When this intersection zone is small compared to the audio wavelength, the cumulative nonlinear interaction between ultrasonic beams is negligible.

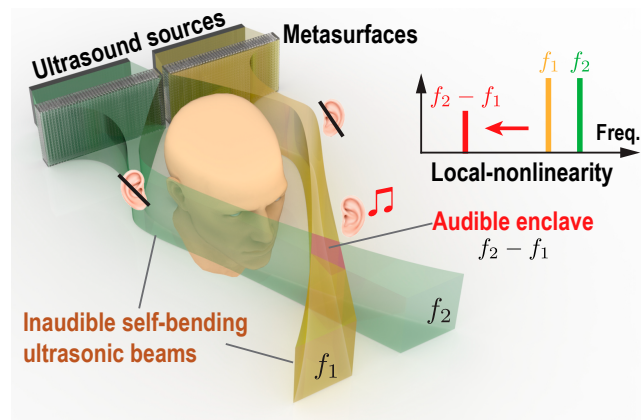


Fig. 1. Schematic depicting the remote creation of an audible enclave at frequency $f = |f_2 - f_1|$ by leveraging the local nonlinear interactions of two self-bending ultrasonic beams at frequencies f_1 and f_2 . Metasurfaces covering ultrasound sources enable the generation of two self-bending ultrasonic beams, culminating in an intersection area behind the obstacle (illustrated as a human head in this figure).

Instead, the local nonlinear interaction dominates, resulting in highly localized audible waves within the intersection zone. The resultant audio sound pressure at frequency $f = |f_2 - f_1|$ can be approximated by (31)

$$p(\mathbf{r}) = \left(\frac{f_1}{f_2} + \frac{f_2}{f_1} - 1 \right) \frac{p_1^*(\mathbf{r}) p_2(\mathbf{r})}{2\rho_0 c_0^2} - \frac{\rho_0}{2} \mathbf{v}_1^*(\mathbf{r}) \cdot \mathbf{v}_2(\mathbf{r}), \quad [1]$$

where the superscript “*” denotes the complex conjugate, ρ_0 is air density, c_0 is the linear sound speed, $p_i(\mathbf{r})$ and $\mathbf{v}_i(\mathbf{r})$ are the sound pressure and particle velocity of ultrasound at frequency of f_i ($i = 1, 2$), respectively.

From Eq. 1, it is seen that the audio sound pressure along the trajectories of the two self-bending beams, except within their intersection zone, is minimal due to the negligible overlap of the ultrasound fields $p_1^* p_2$ ($\mathbf{v}_1^* \cdot \mathbf{v}_2$). Consequently, an audible enclave is remotely generated behind an obstacle with inaudible trajectories from the sound source, meaning that the human head (obstacle) in front of the sound source cannot perceive audible signals. Notably, a major advantage of our proposed concept is its ability to overcome the limit due to diffraction in linear acoustics. Specifically, the spatial resolution (size) of audible enclaves is determined by the ultrasonic waves, which possess much smaller wavelengths compared to the audio waves of interest. Furthermore, a subwavelength aperture size source can create the audible enclaves in the far field defined by the Rayleigh distance, resulting in a compact real-world implementation of this technique.

Design of the Metasurface for Self-bending Ultrasonic Beams.

As illustrated in Fig. 1, two metasurfaces are used in this study to precisely control the phase of two ultrasonic beams emitted by two sound sources. The 3D model and sample photo of one metasurface are shown in Fig. 2 A and B, respectively. Each acoustic metasurface is discretized along the x -direction into 40 unit cells to achieve the required phase profile and repeated along the z -direction for 20 times. The schematic of the air channel of the unit cell, with walls 0.6 mm thick, is depicted in Fig. 2C. Here, the periodicity of unit cell in the xz -plane is set to 4 mm (approximately half the wavelength at $f_u = 40 \text{ kHz}$), while the air channel width w_1 is 2.8 mm (see *SI Appendix*, Fig. S3 for effects of w_1). The total height

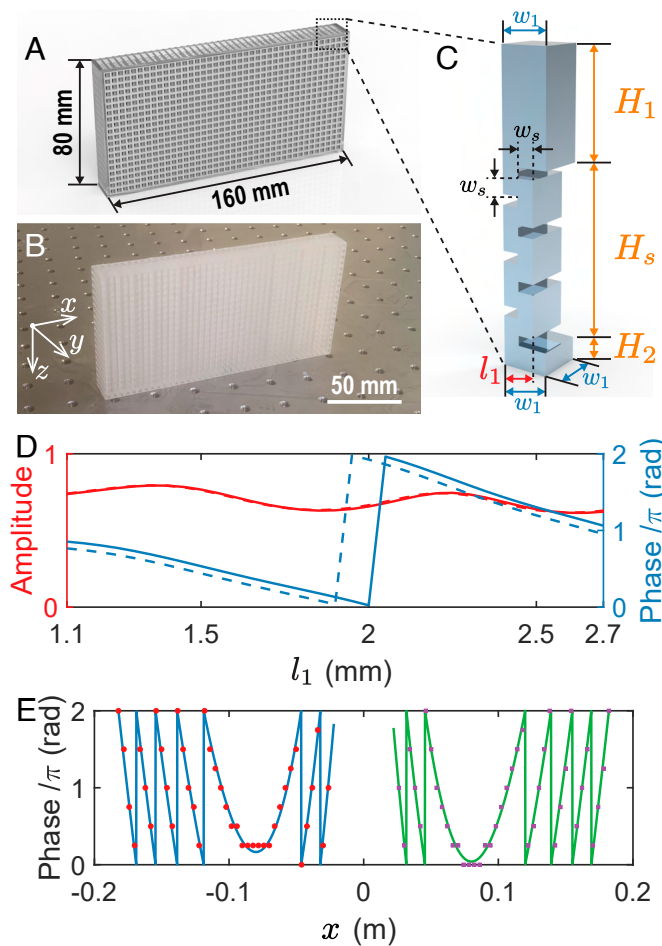


Fig. 2. Metasurfaces for generating self-bending ultrasonic beams. (A) 3D model and (B) sample photo of one metasurface. (C) The schematic and dimensions of the air channel of the unit cell. (D) The amplitude (red lines: —, - - -) and phase (blue lines: —, - - -) of the transmission coefficient of the unit cell as a function of the geometric parameter l_1 . In (D), solid (—, —) and dashed (- - -, - - -) lines represent the metasurfaces designed at 39.5 kHz and 40 kHz, respectively. (E) Continuous (solid lines: —, —) and discrete (markers: ●, □) phase distributions of the metasurfaces. Metasurfaces located in $x < 0$ and $x > 0$ are designed at 39.5 kHz and 40 kHz, respectively.

$H = H_s + H_1 + H_2$ is set to satisfy the Fabry–Perot resonance condition for maximizing the transmission. Specifically, the total height of the unit cell, H , is chosen to be approximately twice the first working wavelength (40), i.e., $H = 18 \text{ mm} \approx 2c_0/f_0$. The zig-zag channel with a height of $H_s = 10.2 \text{ mm}$ is tuned with the parameter l_1 between 1.1 mm and 2.7 mm, modulating the transmitted phase across a complete 2π range as shown in Fig. 2D. While sweeping l_1 , the channel width w_s is fixed as 1 mm to avoid excess thermoviscous loss. The channels labeled with $H_1 = 6.4 \text{ mm}$ and $H_2 = 1.4 \text{ mm}$ are designed by including a wider air channel that matches well with the impedance of free space. As a result, the pressure transmission coefficient is approximately 70% for the frequency of interest, as shown in Fig. 2D. The phase profile provided by the metasurfaces for the self-bending ultrasonic beams (24) is shown in Fig. 2D, where the solid lines represent the continuous phase profile characterized by the equation $\phi(x) = [|x| - 2R_0 \arctan(|x|/R_0)]\omega_i/c_0$, where $\omega_i = 2\pi f_i$, $i = 1, 2$, and the bending radius $R_0 = 80 \text{ mm}$ (which is close to a human head size) and the markers exhibit the discrete phases of 80 elements (40 elements for 39.5 kHz and the other 40 elements for 40 kHz). The self-bending beams used

in this study possess a nonparaxial circular trajectory, enabling them to efficiently bypass a human head (24). Eight different types of elements are chosen to cover the phase shift of 2π range at intervals of $\pi/4$.

Spatial Sound Field Distributions for Pure-Tone Audio Signal Excitations.

We first examine the spatial distribution of the sound field for a pure-tone audio signal excitation. Fig. 3 shows both the measured and simulated sound field distributions (see SI Appendix, Figs. S1 and S2 for more details) (41). Our setup involves two line sources, each with a length of $a = 0.16 \text{ m}$, positioned at line $y = 0$ and covered by metasurfaces. The ultrasound waves emitted by the source located in the region $-a - \Delta a \leq x \leq -\Delta a$ ($\Delta a \leq x \leq \Delta a + a$) are directed toward the $+x$ ($-x$) direction at 39.5 kHz (40 kHz), through the wavefront shaping effects of metasurfaces, forming self-bending beams. Here, $\Delta a = 25 \text{ mm}$ is a small separation chosen for the practical and convenient setup of the experiment. The audible DFW at frequency $f = 500 \text{ Hz}$ is generated in the air due to quadratic acoustic nonlinearity. To obstruct the beams, we place an acoustically rigid cylinder in front of the sources. The cylinder has a radius of $r_0 = 90 \text{ mm}$, a dimension comparable to that of a human head.

Fig. 3 C and E present the measured ultrasound fields, displaying clearly observable self-bending beams as predicted in the simulated results (Figs. 3 D and F). In Fig. 3A, at $(x, y) = (0, 325 \text{ mm})$, we observe a highly localized audio spot

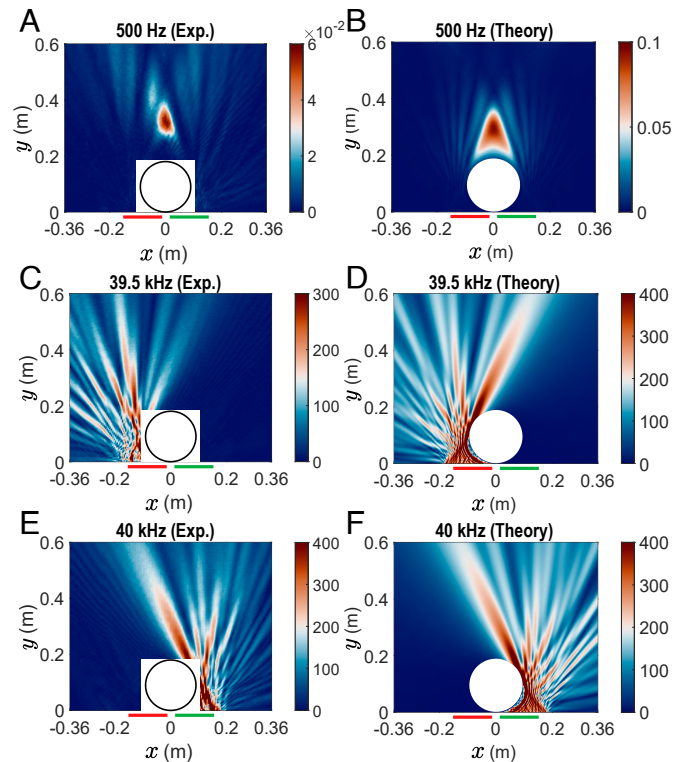


Fig. 3. Sound field distributions (in pascals, Pa) for a pure-tone audio signal excitation. (A and B) Audio sound fields at 500 Hz with an observable audible enclave centered at $(x, y) = (0.325 \text{ mm})$. Self-bending ultrasonic beams at (C and D) 39.5 kHz and (E and F) 40 kHz directed toward the $+x$ and $-x$ directions, respectively. A circular acoustically hard obstacle is placed with its center at $(0, 90 \text{ mm})$ and a radius of 90 mm. Ultrasonic sources at 39.5 kHz (—) and 40 kHz (—) are denoted by two solid lines below $y = 0$. Simulations in (D) and (F) are obtained using COMSOL Multiphysics, while the distribution in (B) is calculated using Eq. 1. (A, C, and E) Measured and (B, D, and F) simulated results.

at the intersection of the main lobes of two ultrasonic beams behind the obstacle. This spot exhibits a deep subwavelength size (0.06 m full width at half maximum sound energy) compared to the audio wavelength at 500 Hz (0.68 m). Such localization arises from local nonlinearity, with the measured results aligning with the predicted ones as shown in Fig. 3B. Notably, the trajectories of two self-bending ultrasonic beams to form audible enclaves remain inaudible. Specifically, the center of the audible enclave (0, 325 mm) in Fig. 3A measures 58.3 mPa (66.3 dB re 20 μPa), while the audio sound pressure at two typical points in the trajectories $x = -105$ mm, $y = 90$ mm and $x = 105$ mm, $y = 90$ mm is only 0.55 mPa (25.8 dB) and 1.7 mPa (35.6 dB), respectively, showcasing remarkable acoustic contrast of 40.5 dB and 30.7 dB. In contrast, as shown in *SI Appendix*, Fig. S6, the audible enclave cannot be generated without using metasurfaces to form the self-bending ultrasonic beams. It is also noted that our proposed approach utilizes the local nonlinearity, which differs from the conventional parametric array (31, 35–37) that rely on cumulative nonlinearity. This distinction is demonstrated in *SI Appendix*, Figs. S7–S10, where the audible enclave is not observed.

It is worth noting that the sound fields are measured in a common room with dimensions of 11.1 m × 5.3 m × 2.4 m (see *SI Appendix*, Fig. S4 for details), ensuring robust performance in the formation of audible enclaves in reverberant environments. The control of long-wavelength audio waves in such indoor environments is crucial yet challenging due to multiple scattering by walls, furniture, and human bodies (11). However, the effects of reverberation on high-frequency ultrasound waves are less significant, as they are rapidly attenuated in air due to thermoviscous and relaxation-induced absorptions (42). Consequently, reflected and scattered ultrasound waves contribute insignificantly to the total sound fields, ensuring that the formation of audible enclaves based on local nonlinear interactions of self-bending ultrasonic beams remains less susceptible to reverberation. Furthermore, the robustness of the audible enclave formation under varying head sizes and displacements is examined, and potential solutions are presented in *SI Appendix*, Figs. S11–S17.

We proceed to evaluate the wideband performance of the proposed audible enclave creation. While humans can detect sound waves across a range from 20 Hz to 20 kHz, the major energy in real-world applications, such as speech communications, is typically found within the 100 Hz to 4 kHz range (1). Therefore, sound fields are measured at the center frequencies of six typical octave bands, ranging from 125 Hz to 4 kHz, as presented in Fig. 4 (see *SI Appendix*, Fig. S2 for corresponding measured ultrasound fields) (41). Remarkably, despite using the same metasurfaces designed at around 40 kHz across different audio frequencies, the audible enclaves are consistently formed at the same location with similar size. Although some small sidelobes formed behind the audible enclave, the trajectory of self-bending ultrasonic beams remained inaudible.

The bandwidth performance of the proposed audible enclaves is determined by both ultrasonic beams and metasurfaces. The diffraction ability of the local-nonlinearity-enabled generation of the DFW depends on short-wavelength ultrasound waves (31). This indicates that the resolution of the generation of the audible enclave is determined by the ultrasound wavelength and can be further enhanced by increasing the ultrasound frequency. In linear acoustics, the working frequency bandwidth of metasurfaces is commonly constrained due to resonance-based mechanisms (39). However, a narrow bandwidth at high frequencies can result in a wide bandwidth at low frequencies. For instance, even though only a 10% bandwidth at 40 kHz is observed in this work, it

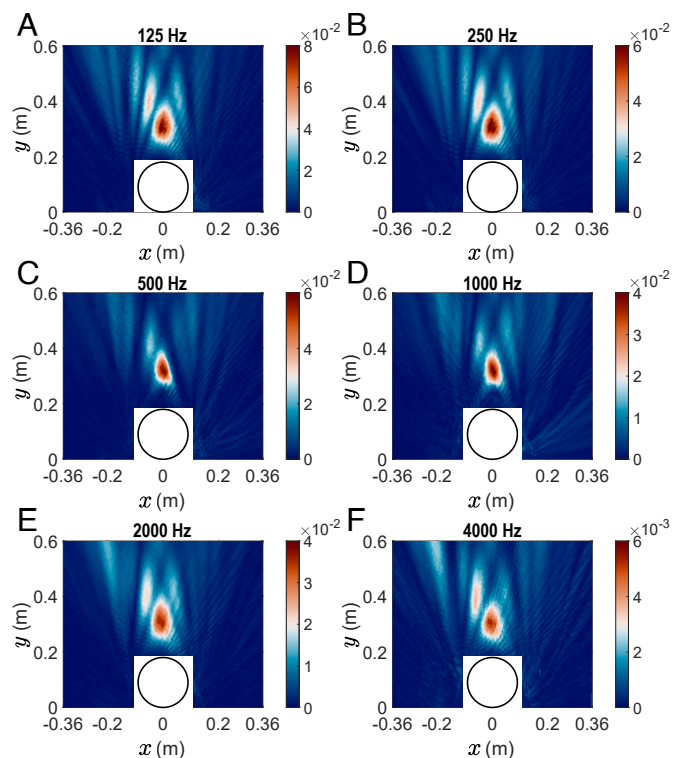


Fig. 4. Measured audio sound field distributions (in pascals, Pa) for pure-tone audio signal excitations in the presence of a circular acoustically hard obstacle with a radius of 90 mm at (A) 125 Hz, (B) 250 Hz, (C) 500 Hz, (D) 1 kHz, (E) 2 kHz, and (F) 4 kHz. In all cases, the center ultrasonic frequency is 40 kHz, and the same metasurfaces used in Fig. 3 are employed.

translates to $40 \text{ kHz} \times 10\% = 4 \text{ kHz}$, which is sufficient for the audible frequency range. The bandwidth limited by metasurfaces can potentially be further improved using more sophisticated designs (43).

Another observation in Fig. 4 is that the energy in audible enclaves decreases as the audible frequency increases. This phenomenon is attributed to the PZT-based ultrasonic emitters (Murata MA40S4S) used in experiments, which feature a narrow-band frequency response around 40 kHz (44). This issue could potentially be addressed by employing high-power wideband micromachined ultrasound transducers (45, 46).

Performance for Transient Wideband Audio Signal Excitations. In real-world audio applications, it is essential to emit transient wideband audio signals, denoted as $s(t)$, such as music reproduction. To create a transient audible enclave, we utilize double sideband amplitude modulation to modulate audio signals onto a pure-tone ultrasound signal with a frequency of f_u , although there exists more sophisticated modulation techniques (36, 47). As shown in Fig. 5, in our design, the signal fed into the right ultrasonic source (referred to as “source R”) is $s_R(t) = \cos(2\pi f_u t)$, where t is the time. For any arbitrary transient audio signal, $s(t)$, the signal fed into the left ultrasonic source (referred to as “source L”) is set as $s_L(t) = s(t) \cos(2\pi f_u t)$. Through Fourier analysis, we find that the spectrum of $s_L(t)$ is $s_L(f) \propto s(f) * [\delta(f - f_u) + \delta(f + f_u)]$, where $*$ is the linear convolution in the frequency domain and $\delta(\cdot)$ denotes the Dirac-delta function. Each audio component in $s(f)$ at frequency f contributes to the spectrum $s_L(f)$, which includes lower and upper sideband components at frequencies $f_u - f$ and $f_u + f$, respectively. Consequently, for a transient audio

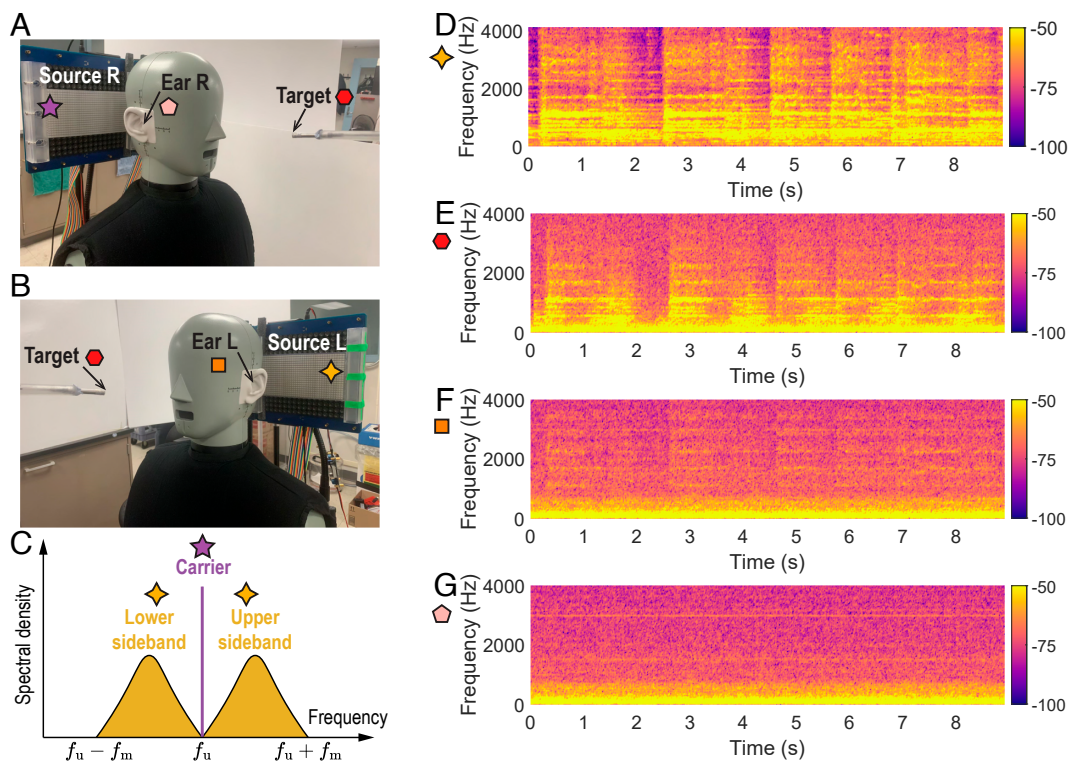


Fig. 5. Measurement with a transient wideband audio signal excitation. (A) Right and (B) Left profile views of measurement setup in the presence of a head and torso simulator. (C) Illustration of the spectral density of excitation signals. (D–G) Spectrograms (dB/Hz): (D) the transient wideband audio excitation signal; (E) measured signals at the target spot; (F) measured signals at ear L; (G) measured signals at ear R.

signal with a maximal frequency of f_m , sidebands ranging from $(f_u - f_m, f_u + f_m)$ are emitted, as illustrated in Fig. 5C. When the maximal audible frequency is small compared to the carrier frequency, such as $f_m = 4\text{ kHz}$ and $f_u = 40\text{ kHz}$, the transient ultrasonic beams can still effectively interact with the metasurfaces. At the intersection of two ultrasonic self-bending beams, the local nonlinear interactions of the ultrasound at frequency f_u generated by source R and that at sidebands $(f_u \pm f)$ emitted by source L form a transient audible enclave.

To assess the performance of transient wideband excitation, we utilize a 9-s sample of audio signal (loaded built-in data ‘handel’ in MATLAB R2023a) with its spectrogram depicted in Fig. 5D (Movie S1) (41). Additionally, as shown in Fig. 5A and B, we place a head and torso simulator (HATS, Brüel and Kjær Type 4128) in front of the source to simulate a listener as the obstacle. In Fig. 5E, a spectrogram resembling that of the excitation signal is measured at the target spot situated at the center of the audible enclave. The attenuation of amplitude at higher frequencies, compared to lower frequencies, is attributed to the narrow frequency bandwidth of the PZT-based ultrasonic transducers, as discussed previously. Notably, the audio energy measured at both ears of the HATS, shown in Fig. 5F and G, is significantly lower than that at the audible enclave across the wideband frequency range. Some weak audio energies are observed at the *Left* ear (Fig. 5F), primarily due to the nonlinear interaction of sidebands themselves generated by the left source. This can be further mitigated by reducing the energy of sideband signals while increasing the energy of the carrier signal. Nonetheless, these components (Fig. 5F) are already at least 20 dB lower than those measured at the target spot in the audible enclave (Fig. 5E), which suffices for most audio applications.

Discussion

By marrying local acoustic nonlinearity with inaudible self-bending ultrasonic beams, we have successfully created an audible enclave for remotely delivering sound content to a targeted zone without causing disturbances to listeners even along the beam’s trajectory. Furthermore, we have showcased the remarkable wideband capabilities of cost-effective metasurfaces when subjected to transient audio signals covering 6 octave bands, spanning from 125 Hz to 4 kHz. The formation of our proposed audible enclave overcomes the diffraction limit imposed on long-wavelength audio waves. By leveraging acoustic local nonlinearity, we achieve ultrafine audio wave manipulation with a resolution comparable to the ultrasonic wavelength through precise engineering of ultrasonic beams. The compact implementation size (0.16 m) and robust formation of audio enclaves within a common reverberant room further underscore the practicality of our proposed technique. Additionally, the proposed audible enclaves can be potentially utilized to create quiet zones by canceling out original noise fields with minimal disruptions to surrounding areas. Achieving this in traditional active noise control systems presents considerable challenges (13, 48).

In pursuit of more practical applications of our proposed technique, we acknowledge a key challenge is the nonlinear distortion, which can degrade audio quality, particularly in high-fidelity wideband sound reproduction. This distortion stems from the inherent nonlinear nature of our technique. However, we believe that the distortion can be effectively mitigated in the future through nonlinear compensation techniques leveraging classical nonlinear filters and data-driven deep learning approaches (49, 50). Another concern relates to the low power conversion efficiency from carrier ultrasound waves to audio waves. As per Eq. 1, the resultant audio sound pressure can be approximated as

$|p_0|^2/(2\rho_0c_0^2)$, assuming $p_0 = p_1 \approx p_2$. To achieve typical audio sound pressure levels (ranging from 2.8 to 279 mPa, equivalent to 40 to 80 dB re 20 μPa) in most audio applications, ultrasound pressure levels of $p_0 = 28$ to 282 Pa (120 to 140 dB) are required. While such high-intensity airborne ultrasound levels are inaudible to most listeners, they raise potential safety concerns. The ICNIRP statement (51) highlights that there is variability in human sensitivity to ultrasound, with certain individuals perceiving ultrasonic tones at thresholds as low as 120 dB SPL at 40 kHz. It also acknowledges that nonspecific symptoms, such as ear pressure, discomfort, and fatigue, can occur at SPLs exceeding 120 to 130 dB for higher ultrasonic frequencies. However, the statement emphasizes that robust dose-response relationships and reliable health impact studies at these frequencies remain limited.

From an energy perspective, ultrasound intensity can be estimated using $W = |p_0|^2/(2\rho_0c_0)$ (52), resulting in a range of 0.09 to 9.58 mW/cm² for the aforementioned range of 120 to 140 dB. Human skin reflects approximately 99.9% of airborne ultrasonic energy due to the significant acoustic impedance mismatch (53), allowing only 0.09 to 9.58 $\mu\text{W}/\text{cm}^2$ to enter the body at maximum. The Food and Drug Administration (FDA) standards set limits of 720 mW/cm² for fetal, cardiac, and vascular imaging and 50 mW/cm² for ophthalmic imaging (54). The airborne ultrasound pressure level range 120 to 140 dB exhibits a safety margin over 1/5200 in comparison to the FDA limits. Therefore, the primary risk of ultrasound exposure, in practical terms, lies in potential effects on hearing, resulting in temporary or permanent hearing threshold shifts and other subjective effects (51, 55, 56). Although quantifying and analyzing these effects currently remain challenging, researchers generally agree that they are less likely to occur at higher ultrasound frequencies. From Eq. 1, the audio sound pressure is typically independent of ultrasound frequency. Thus, increasing the carrier ultrasound frequency can potentially reduce risks in real-world applications.

Materials and Methods

Hardware of Ultrasound Sources. We construct two ultrasound arrays, labeled as sources L and R in Fig. 5. Each array consists of $16 \times 16 = 256$ PZT-based ultrasonic transducers (Murata MA40S4S) with a diameter of 10 mm and a center frequency of 40 kHz (see *SI Appendix*, Figs. S4 and S5 for more details). During experiments, however, only the central 8 rows ultrasonic transducers are activated and covered by metasurfaces, as shown in Fig. 5 A and B. All activated transducers emit in-phase ultrasound waves, with their initial phases calibrated using a field-programmable gate array (Xilinx XC7A100T).

1. J. Benesty, M. M. Sondhi, Y. Huang, Eds., *Springer Handbook of Speech Processing* (Springer, Berlin, London, 2008).
2. Y. H. Kim, J. W. Choi, *Sound Visualization and Manipulation* (Wiley, Singapore, 2013).
3. B. Rafaely, *Fundamentals of Spherical Array Processing*, Springer Topics in Signal Processing (Springer, Berlin Heidelberg, Berlin, Heidelberg, 2015), vol. 8.
4. T. Betlehem, W. Zhang, M. A. Poletti, T. D. Abhayapala, Personal sound zones: Delivering interface-free audio to multiple listeners. *IEEE Sig. Process. Mag.* **32**, 81–91 (2015).
5. P. N. Samarasinghe, W. Zhang, T. D. Abhayapala, Recent advances in active noise control inside automobile cabins: Toward quieter cars. *IEEE Sig. Process. Mag.* **33**, 61–73 (2016).
6. V. Välimäki, J. D. Reiss, All about audio equalization: Solutions and frontiers. *Appl. Sci.* **6**, 129 (2016).
7. J. Y. Hong, J. He, B. Lam, R. Gupta, W. S. Gan, Spatial audio for soundscape design: Recording and reproduction. *Appl. Sci.* **7**, 627 (2017).
8. J. Y. Hong *et al.*, Quality assessment of acoustic environment reproduction methods for cinematic virtual reality in soundscape applications. *Build. Environ.* **149**, 1–14 (2019).
9. M. R. Bai, C. C. Lee, Development and implementation of cross-talk cancellation system in spatial audio reproduction based on subband filtering. *J. Sound Vib.* **290**, 1269–1289 (2006).

Fabrication of Metasurfaces. The samples are fabricated using a commercial stereolithography 3D printer (Formlabs Form 3L, the lateral resolution is 0.025 mm). The 3D printed samples are rinsed in IPA in Form Wash for 30 min and then postcured by 405 nm and 375 nm light in Form Cure for 1 h.

Simulations. The simulations in the ultrasonic frequency range are conducted using the commercial finite element analysis software COMSOL Multiphysics v6.0 with the "Pressure Acoustics, Frequency Domain" module. The thermoviscous loss inside the metasurface is modeled using "Thermoviscous Boundary Layer Impedance" boundary condition. Acoustically rigid boundaries are assigned to the walls of the solid materials in the metasurfaces. The background medium is considered to be air with a mass density (ρ_0) of 1.21 kg/m³ and a sound speed (c_0) of 343 m/s. Due to memory constraints, only one unit cell along the z-direction is simulated. A "Periodic Condition" with "Continuity" is applied along the z-direction to approximate the 20 repeats in experiments. The audio sound field is obtained by substituting the ultrasound fields obtained in COMSOL into Eq. 1.

Experimental Settings and Sound Measurement. The experiments are conducted in our laboratory, which is approximately a cuboid room with dimensions of 11.1 m \times 5.3 m \times 2.4 m (*SI Appendix*, Fig. S4). Spatial sound field distributions depicted in Figs. 3 A-C and 4 are measured using a single microphone (GRAS Type 40BF), which is mounted on a programmable scanning stage to scan the sound field. The measurement region forms a rectangle lying in the horizontal plane intersecting the center of the sources. As shown in Fig. 3, two ultrasonic sources are located along the line $y = 0$ within the region $-185 \text{ mm} \leq x \leq -25 \text{ mm}$ and $25 \text{ mm} \leq x \leq 185 \text{ mm}$. The measurement region covered an area of $-360 \text{ mm} \leq x \leq 360 \text{ mm}$ and $0 \leq y \leq 600 \text{ mm}$, with a spatial resolution of 5 mm in both the x- and y-directions. A section within a rectangle ($-105 \text{ mm} \leq x \leq 105 \text{ mm}$ and $0 \leq y \leq 185 \text{ mm}$) is not measured due to the presence of the obstacle, left blank in Figs. 3 and 4. All signals are acquired using National Instruments Data Acquisition hardware PCIe-6353. To simulate a listener, a head and torso simulator (HATS, Brüel and Kjær Type 4128) is employed, as shown in Fig. 5 A and B. Two microphones are positioned at both the *Left* and *Right* ears of the HATS to capture the transient audio signal, as depicted in Fig. 5 F and G.

Data, Materials, and Software Availability. *wav, *mat, and *m files have been deposited in Zenodo (<https://zenodo.org/records/14873417>; DOI: 10.5281/zenodo.14873417) (41).

ACKNOWLEDGMENTS. This work was supported by the Startup funds from The Pennsylvania State University and NSF award 2401236. X.X. acknowledges the financial support from Lawrence Livermore National Laboratory's Lab Directed Research and Development Program (22-ERD-004). Work at Lawrence Livermore National Laboratory was performed under the auspices of the U.S. Department of Energy by Lawrence Livermore National Laboratory under Contract DE-AC52-07NA27344. We gratefully acknowledge Dr. Michelle Vigeant-Haas and her team at The Pennsylvania State University for generously providing the head and torso simulator used in this study.

10. J. H. Chang, J. Y. Park, Y. H. Kim, Scattering effect on the sound focused personal audio system. *J. Acoust. Soc. Am.* **125**, 3060–3066 (2009).
11. G. Ma, X. Fan, P. Sheng, M. Fink, Shaping reverberating sound fields with an actively tunable metasurface. *Proc. Natl. Acad. Sci. U.S.A.* **115**, 6638–6643 (2018).
12. R. M. Sullenberger, S. Kaushik, C. M. Wynn, Photoacoustic communications: Delivering audible signals via absorption of light by atmospheric H₂O. *Opt. Lett.* **44**, 622–625 (2019).
13. J. Zhong *et al.*, Quiet zone generation in an acoustic free field using multiple parametric array loudspeakers. *J. Acoust. Soc. Am.* **151**, 1235–1245 (2022).
14. H. Zhang, Q. Wang, M. Fink, G. Ma, Optimizing multi-user indoor sound communications with acoustic reconfigurable metasurfaces. *Nat. Commun.* **15**, 1270 (2024).
15. G. A. Siviloglou, J. Broky, A. Dogariu, D. N. Christodoulides, Observation of accelerating Airy beams. *Phys. Rev. Lett.* **99**, 213901 (2007).
16. P. Zhang *et al.*, Nonparaxial Mathieu and Weber accelerating beams. *Phys. Rev. Lett.* **109**, 193901 (2012).
17. P. Zhang *et al.*, Generation of acoustic self-bending and bottle beams by phase engineering. *Nat. Commun.* **5**, 4316 (2014).

18. T. Illovitsh, A. Illovitsh, J. Foiret, K. W. Ferrara, Imaging beyond ultrasonically-impenetrable objects. *Sci. Rep.* **8**, 5759 (2018).
19. X. Chen *et al.*, Ultrasonic imaging based on pulsed Airy beams. *IEEE Trans. Ultrason. Ferroelectr. Freq. Control* **70**, 1146–1156 (2023).
20. Z. Hu, Y. Yang, L. Xu, Y. Jing, H. Chen, Airy-beam-enabled binary acoustic metasurfaces for underwater ultrasound-beam manipulation. *Phys. Rev. Appl.* **18**, 024070 (2022).
21. K. Mohanty, S. Mahajan, G. Pinton, M. Muller, Y. Jing, Observation of self-bending and focused ultrasound beams in the megahertz range. *IEEE Trans. Ultrason. Ferroelectr. Freq. Control* **65**, 1460–1467 (2018).
22. H. Gao *et al.*, Acoustic focusing by symmetrical self-bending beams with phase modulations. *Appl. Phys. Lett.* **108**, 073501 (2016).
23. S. Pu *et al.*, Auto-focusing acoustic-vortex tweezers for obstacle-circumventing manipulation. *J. Appl. Phys.* **130**, 234903 (2021).
24. S. Zhao *et al.*, Delivering sound energy along an arbitrary convex trajectory. *Sci. Rep.* **4**, 6628 (2014).
25. M. F. Simón-Gálvez, S. J. Elliott, J. Cheer, The effect of reverberation on personal audio devices. *J. Acoust. Soc. Am.* **135**, 2654–2663 (2014).
26. J. Zhu *et al.*, A holey-structured metamaterial for acoustic deep-subwavelength imaging. *Nat. Phys.* **7**, 52–55 (2011).
27. N. Kaina, F. Lemoult, M. Fink, G. Lerosey, Negative refractive index and acoustic superlens from multiple scattering in single negative metamaterials. *Nature* **525**, 77–81 (2015).
28. C. Shen *et al.*, Broadband acoustic hyperbolic metamaterial. *Phys. Rev. Lett.* **115**, 254301 (2015).
29. Y. X. Shen *et al.*, Ultrasonic super-oscillation wave-packets with an acoustic meta-lens. *Nat. Commun.* **10**, 3411 (2019).
30. G. Ma *et al.*, Towards anti-causal Green's function for three-dimensional sub-diffraction focusing. *Nat. Phys.* **14**, 608–612 (2018).
31. J. Zhong *et al.*, Local-nonlinearity-enabled deep subdiffraction control of acoustic waves. *Phys. Rev. Lett.* **131**, 234001 (2023).
32. M. F. Hamilton, D. T. Blackstock, *Nonlinear Acoustics* (Acoustical Society of America, New York, 2008).
33. F. A. Duck, Nonlinear acoustics in diagnostic ultrasound. *Ultrasound Med. Biol.* **28**, 1–18 (2002).
34. J. Gu, Y. Jing, Modeling of wave propagation for medical ultrasound: A review. *IEEE Trans. Ultrason. Ferroelectr. Freq. Control* **62**, 1979–1992 (2015).
35. P. J. Westervelt, Parametric acoustic array. *J. Acoust. Soc. Am.* **35**, 535–537 (1963).
36. W. S. Gan, J. Yang, T. Kamakura, A review of parametric acoustic array in air. *Appl. Acoust.* **73**, 1211–1219 (2012).
37. J. Zhong, X. Qiu, *Acoustic Waves Generated by Parametric Array Loudspeakers* (CRC Press, Boca Raton, 2024).
38. S. I. Aanonsen, T. Barkve, J. N. Tjøtta, S. Tjøtta, Distortion and harmonic generation in the nearfield of a finite amplitude sound beam. *J. Acoust. Soc. Am.* **75**, 749–768 (1984).
39. B. Assouar *et al.*, Acoustic metasurfaces. *Nat. Rev. Mater.* **3**, 460–472 (2018).
40. Y. Zhu *et al.*, Systematic design and experimental demonstration of transmission-type multiplexed acoustic metaholograms. *Adv. Funct. Mater.* **31**, 2101947 (2021).
41. J.-X. Zhong, Source files and data for the paper "Audible enclaves crafted by nonlinear self-bending ultrasonic beams". Zenodo. <https://zenodo.org/records/14873417>. Deposited 1 March 2025.
42. J. Zhong, H. Zou, J. Lu, A modal expansion method for simulating reverberant sound fields generated by a directional source in a rectangular enclosure. *J. Acoust. Soc. Am.* **154**, 203–216 (2023).
43. X. Fan *et al.*, Ultrabroadband and reconfigurable transmissive acoustic metascreen. *Adv. Funct. Mater.* **33**, 2300752 (2023).
44. A. Jager, "Airborne Ultrasound Phased Arrays," PhD thesis, Technical University of Darmstadt, Darmstadt, Germany (2019).
45. Y. Je, H. Lee, W. Moon, The impact of micromachined ultrasonic radiators on the efficiency of transducers in air. *Ultrasonics* **53**, 1124–1134 (2013).
46. X. Niu *et al.*, An air-coupled electrostatic ultrasound transducer using a MEMS microphone architecture. *J. Microelectromech. Syst.* **31**, 813–819 (2022).
47. R. G. Gallager, *Principles of Digital Communication* (Cambridge University Press, 2008).
48. N. Tanaka, M. Tanaka, Active noise control using a steerable parametric array loudspeaker. *J. Acoust. Soc. Am.* **127**, 3526–3537 (2010).
49. C. Shi, Y. Kajikawa, Volterra model of the parametric array loudspeaker operating at ultrasonic frequencies. *J. Acoust. Soc. Am.* **140**, 3643–3650 (2016).
50. O. Nelles, *Nonlinear System Identification: From Classical Approaches to Neural Networks, Fuzzy Models, and Gaussian Processes* (Springer, ed. 2, 2022).
51. K. Karipidis *et al.*, Validity of the 1984 interim guidelines on airborne ultrasound and gaps in the current knowledge. *Health Phys.* **127** 326–347 (2023).
52. A. D. Pierce, *Acoustics: An Introduction to Its Physical Principles and Applications* (Springer Nature, Cham, Switzerland, ed. 3, 2019).
53. G. D. Ludwig, The velocity of sound through tissues and the acoustic impedance of tissues. *J. Acoust. Soc. Am.* **22**, 862–866 (1950).
54. T. R. Nelson, J. B. Fowlkes, J. S. Abramowicz, C. C. Church, Ultrasound biosafety considerations for the practicing sonographer and sonologist. *J. Ultrasound Med.* **28**, 139–150 (2009).
55. B. C. Moore, *An Introduction to the Psychology of Hearing* (Brill NV, Leiden, The Netherlands, ed. 6., 2013).
56. A. Di Battista *et al.*, The effects of high-intensity 40 kHz ultrasound on cognitive function. *Appl. Acoust.* **200**, 109051 (2022).